

See discussions, stats, and author profiles for this publication at: <https://www.researchgate.net/publication/235331519>

Morphology-Controlled Synthesis of Nanocrystalline η -Al₂O₃ Thin Films, Powders, Microbeads, and Nanofibers with Tunable Pore Sizes from Preformed Oligomeric Oxo-Hydroxo Building Bl...

ARTICLE in CHEMISTRY OF MATERIALS · DECEMBER 2011

Impact Factor: 8.35 · DOI: 10.1021/cm202692q

CITATIONS

15

READS

86

8 AUTHORS, INCLUDING:



Christoph Weidmann

Justus-Liebig-Universität Gießen

10 PUBLICATIONS 113 CITATIONS

SEE PROFILE



Jan Haetge

University of Münster

14 PUBLICATIONS 333 CITATIONS

SEE PROFILE



Bernd M Smarsly

Justus-Liebig-Universität Gießen

215 PUBLICATIONS 8,187 CITATIONS

SEE PROFILE



Torsten Brezesinski

Karlsruhe Institute of Technology

92 PUBLICATIONS 3,264 CITATIONS

SEE PROFILE

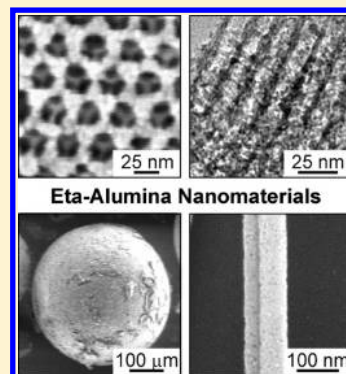
Morphology-Controlled Synthesis of Nanocrystalline η -Al₂O₃ Thin Films, Powders, Microbeads, and Nanofibers with Tunable Pore Sizes from Preformed Oligomeric Oxo-Hydroxo Building Blocks

Christoph Weidmann,[†] Kirstin Brezesinski,[†] Christian Suchomski,[†] Kristin Tropp,[†] Natascha Grosser,[†] Jan Haetge,[†] Bernd M. Smarsly,^{*,†} and Torsten Brezesinski^{*,†}

[†]Institute of Physical Chemistry, Justus-Liebig-University Giessen, Heinrich-Buff Ring 58, Giessen 35392, Germany

S Supporting Information

ABSTRACT: Herein the synthesis and characterization of nanocrystalline η -Al₂O₃ materials with different morphologies, including dense nanofibers, hierarchically porous microbeads, and highly ordered mesoporous thin films and powders is reported. These materials were fabricated by facile polymer templating, nanocasting, and electrospinning routes using preformed aluminum-oxo-hydroxo species as the building blocks. We show that the oligomeric building blocks used in this work can be formed under nonaqueous conditions with benzyl alcohol as the oxygen donor and further converted to the eta-phase of Al₂O₃ at temperatures above 700 °C. Electron microscopy, X-ray diffraction, grazing incidence small-angle X-ray scattering, X-ray photoelectron spectroscopy, and physisorption studies collectively verify that the different η -Al₂O₃ materials are well-defined at the nanoscale and the microscale after annealing in air at temperatures as high as 1000 °C. In addition, data obtained on polymer-templated thin films show that both cubic and 2D-hexagonal structures with large pore sizes between 10 and 30 nm can be achieved. These data also show that the conversion of the initially amorphous frameworks comes at little cost to the ordering of the pore-solid architectures. Overall, we believe that the synthesis parameters described here provide a blueprint for future nanomaterials.



KEYWORDS: alumina, catalysis, self-assembly, electrospinning, nanocasting, mesoporous, nanocrystalline

INTRODUCTION

Aluminum oxide with the chemical formula Al₂O₃ is a material of great scientific and technological interest and is known to have a large number of polymorphs.^{1,2} For example, the thermodynamically stable bulk phase, α -Al₂O₃, also referred to as corundum, is a widely studied catalyst support due to its high thermal, chemical, and mechanical stability.^{3–5} Apart from corundum, which is catalytically inert, the different metastable transition phases of Al₂O₃ hold great potential for catalytic applications (i.e., as catalysts and catalytic support materials).^{6–8} We note that the catalytic properties are mainly determined both by surface acidity, which is closely related to the atomic structure, and by textural properties, such as specific surface area and porosity/pore volume. The latter are known to have a profound effect on the surface site density and macrokinetics, respectively.

For nanocrystalline materials with specific surface areas larger than 125 m²·g^{−1} and crystalline domain sizes smaller than 13 nm, γ -Al₂O₃ is the thermodynamically preferred polymorph due to its lower surface energy.⁹ In recent years, it has been shown that γ -Al₂O₃ can be readily formed by thermal decomposition of γ -AlO(OH), also referred to as boehmite.^{10–12} However, other synthesis routes have also been developed in an attempt to prepare nanosized γ -Al₂O₃ materials with high surface areas, such as the nanocasting of lyotropic

liquid crystal phases, the hard-templating method (i.e., confined growth inside a rigid material), and various solvothermal approaches.^{13–21} All of these wet chemical routes have in common that they represent bottom-up approaches, which make use of the stability of the gamma-phase on the nanometer level.

Apart from γ -Al₂O₃, which is the most important alumina-based support material, there are also other metastable transition phases, such as η -Al₂O₃, which hold great promise for catalytic applications, e.g., in petroleum refinement. For example, the exceptional activity of η -Al₂O₃ for isomerization of terminal olefins is well documented in the literature and can be attributed to the high acidity of the catalytically active sites.²² As mentioned above, the acidity is related to the atomic structure, which is the reason why η -Al₂O₃ exhibits a higher catalytic activity than γ -Al₂O₃ in many reactions with industrial relevance, including cracking of 2,4-dimethylpentane and isomerization of 1-pentene and *p*-xylene.⁸

Bulk η -Al₂O₃ can be prepared by thermal dehydration of α -Al(OH)₃, also referred to as bayerite, a method used by Zhang et al. for the synthesis of mesoporous versions of this

Received: September 9, 2011

Revised: November 25, 2011

Published: December 6, 2011

oxide.²³ Zhang et al. presented a two-step process based on the formation of mesostructured bayerite at 100 °C and subsequent thermolysis to η -Al₂O₃ at temperatures above 400 °C. The materials thus obtained show both high specific surface area and large pore volume; however, the pore size of only ~2 nm was rather small. Such small nanopore cavities can impede the mass transport through the bulk of the material, thereby limiting the applicability. Also, the synthesis procedure itself, although very elegant, does not seem to be readily extendable to η -Al₂O₃ materials with larger pores and other morphologies.

To overcome these limitations, we have developed a route that allows η -Al₂O₃ nanomaterials with different morphologies to be produced by using preformed aluminum-oxo-hydroxo species as building blocks. These oligomeric compounds can be synthesized in benzyl alcohol and lend themselves to the fabrication of nanocrystalline η -Al₂O₃ with high thermal stability. In order to demonstrate the versatility of our approach, we show four different types of morphologies in this work: dense nanofibers, hierarchically porous microbeads,²⁴ and highly ordered mesoporous thin films and powders.

The materials in film and powder format were templated using amphiphilic polymers, including Pluronic F127 and P123, KLE,²⁵ and PIB_{*x*}-*b*-PEO_{*y*} with different block lengths. We establish both that the pore size can be readily tuned from approximately 10 to 30 nm and that the different pore-solid architectures can be retained up to annealing temperatures as high as 1000 °C. Since purely mesoporous materials are often only of academic interest, we also show the hard-templating^{25–28} synthesis of micrometer-sized η -Al₂O₃ beads with hierarchical porosity.²⁴ These nanocrystalline beads might be of interest for catalytic and other applications because of the multimodal porosity and the fact that they can be easily handled. Lastly, we report the preparation of nanofibers with 70 nm average diameter and a few tens of micrometers in length by electrospinning.^{29,30}

■ EXPERIMENTAL SECTION

Materials. Anhydrous AlCl₃ (99.9%), 1,3-propanediol (99.6%), anhydrous benzyl alcohol (99.8%), Amberlite XAD-16 polystyrene beads, and Pluronic P123/F127 were purchased from Sigma-Aldrich. Both H[(CH₂CH₂)_{0.67}(CH₂CHCH₂CH₃)_{0.33}]₈₉(OCH₂CH₂)₇₉OH, referred to as KLE, and H[C(CH₃)₂CH₂]_{*x*}C₆H₄(OCH₂CH₂)_{*y*}OH, referred to as PIB_{*x*}-*b*-PEO_{*y*}, were obtained from BASF SE. Polyvinyl butyral (Mowital B 60 H) was donated by Kuraray Europe GmbH.

Synthesis of Building Blocks. In a water-free container, 3.0 g of anhydrous AlCl₃ is dissolved in 10 mL of absolute ethanol and then combined with 0.5 mL of 1,3-propanediol in 40 mL of anhydrous benzyl alcohol. The container is loosely sealed, and the final solution is heated at 80 °C for 12 h. The formed aluminum-oxo-hydroxo species are then precipitated in 300 mL of diethyl ether, isolated by centrifugation, and washed several times with diethyl ether. Lastly, the white powder is dried in air under ambient conditions. The obtained material can be redispersed in methanol, yielding a transparent sol with a solid content of up to 200 mg/mL. The solid content was determined by heating the mixture to 600 °C in air.

Synthesis of Thin Films and Powders. A mixture of 60 mg of KLE (or 60 mg of Pluronic P123; or 120 mg of PIB₅₃-*b*-PEO₄₅, PIB₁₀₇-*b*-PEO₁₀₀, and Pluronic F127, respectively) dissolved in 0.5 mL of methanol (tetrahydrofuran for PIB₁₀₇-*b*-PEO₁₀₀) and 0.2 mL of double distilled water is added to 1.5 mL of the transparent sol with a solid content of ~40 mg/mL. Once the solution is homogeneous, thin films can be produced via dip-coating on polar substrates, including glass and (100)-oriented silicon wafers. Optimal conditions include relative humidities of more than 80% and 40% for KLE-templated and Pluronic-templated thin films, respectively. Powder material is produced in a Petri dish with 120 mg of KLE (or 180 mg of PIB₅₃-

b-PEO₄₅) but under otherwise identical conditions. For best results, both thin film and powder samples are aged at 80 °C for 8 h and then annealed in air using a 6 h ramp to 300 °C followed by another aging for 12 h. Removal of the organic template and crystallization of the initially amorphous frameworks is achieved by heating the materials to 900 °C in air using a rate of 10 °C/min.

Synthesis of Microbeads. 2.0 g of Amberlite XAD-16 polystyrene beads are washed several times with a mixture of water and methanol and then combined with 2.0 mL of the transparent sol with a solid content of ~200 mg/mL. Excess solution that is not drawn into the beads is removed by washing with isopropyl alcohol. The infiltrated material is then dried at 40 °C (infiltration and drying is repeated twice) followed by calcination at 700 °C for 5 h under nitrogen atmosphere. Lastly, the beads are heated to temperatures above 700 °C in air to fully remove the organic template.

Synthesis of Nanofibers. In a typical procedure, 2.5 mL of the transparent sol with a solid content of ~80 mg/mL is combined with 240 mg of 10 wt.% polyvinyl butyral in isopropyl alcohol. Nanofibers can be produced via electrospinning on (100)-oriented silicon wafers and aluminum foil. Optimal conditions include a relative humidity of ~30%. Both combustion of the polyvinyl butyral and crystallization of the inorganic material are achieved by heating the nanofibers to 900 °C in air using a rate of 10 °C/min.

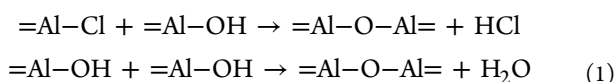
Methods. Bright-field transmission electron microscopy (TEM) and scanning electron microscopy (SEM) images were taken with a CM30-ST microscope from Philips and a LEO Gemini 982, respectively. Atomic force microscopy (AFM) images were collected on a multimode atomic force microscope from Veeco Instruments, employing Olympus microcantilevers (resonance frequency, 300 kHz; force constant, 42 N/m). Wide-angle X-ray diffraction (WAXD) measurements were carried out on an X'Pert PRO diffractometer from PANalytical instruments. Grazing incidence small-angle X-ray scattering (GISAXS) data were collected at the German synchrotron radiation facility HASYLAB at DESY on beamline BW4 using a MarCCD area detector and a sample–detector distance of 1820 mm. X-ray photoelectron spectroscopy (XPS) spectra were acquired on a Physical Electronics ESCA 5600 spectrometer with monochromatic Al-*K* α X-ray source and a multichannel detector OmniIV. The electron takeoff angle to the sample surface was adjusted to 45°. The C1s signal from adventitious hydrocarbon at 284.6 eV was used as the energy reference to correct for charging. Nitrogen and krypton physisorption measurements were conducted at 77 and 87 K, respectively, using the Autosorb-1-MP automated gas adsorption station from Quantachrome Corporation. The film thickness was determined with an Alpha Step IQ Surface Profiler from KLA Tencor. Electrospinning was carried out in a self-built setup consisting of high-voltage power supply (Spellman CZE1000R) and KDS 100 syringe pump (KDS Scientific). The applied electrical field was ~1.3 kV/cm, and the distance from the needle tip to the collector was adjusted to 6 cm. Dynamic light scattering (DLS) was carried out on a Nanotrak Particle Size Analyzer from Microtrac (PMX 200C) at a scattering angle of 180°. A Bruker IFS 48 Fourier transform infrared spectrometer (FTIR) was used to collect IR spectra in attenuated total reflection (ATR) mode. ¹H NMR (nuclear magnetic resonance) spectra were obtained in chloroform-*d* on a Bruker AM 400 spectrometer. Tetramethylsilane (TMS) was used as the internal standard. Thermogravimetric analysis (TGA) data were obtained with a Netzsch STA 409 PC at a heating rate of 5 °C/min. The thermobalance was coupled to a Balzers QMG 421 quadrupole mass spectrometer. The ionization energy was 70 eV. Gas chromatography–mass spectrometry (GC-MS) data were recorded with an Agilent 5973 MSD with 6890 gas chromatograph.

■ RESULTS AND DISCUSSION

The classical synthesis of η -Al₂O₃ involves thermal dehydration of α -Al(OH)₃, as shown in ref 23. This route, however, is not advantageous for the fabrication of mesoporous materials whether in the form of thin films or powders since the pore network might suffer from solid–solid conversion to η -Al₂O₃.

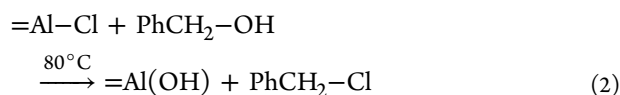
Other forms of aluminum hydroxide or oxide hydroxide, such as gibbsite, boehmite, and pseudoboehmite, can also be converted to Al_2O_3 at elevated temperatures but produce other polymorphs.¹ In contrast, our synthesis route makes use of preformed aluminum-oxo-hydroxo building blocks which directly lead to nanocrystalline $\eta\text{-Al}_2\text{O}_3$ at annealing temperatures above 700 °C.

The oligomeric material employed in this work was synthesized under nonaqueous conditions with benzyl alcohol as the oxygen donor.^{31–33} Briefly, a mixture of benzyl alcohol and 1,3-propanediol, the latter acting as a stabilizing ligand, is added to an ethanolic solution of anhydrous AlCl_3 . After stirring the solution for 12 h at 80 °C, aluminum-oxo-hydroxo species can be precipitated in apolar organic solvents, dried in air, and readily redispersed in various alcoholic solvents. Overall, this method represents a nonaqueous sol–gel route in organic solvents. Al-OH groups are formed *in situ* during synthesis, which then undergo condensation reactions with either chloride substituents or hydroxyl groups according to³⁴



The oligomeric material thus obtained mainly consists of aluminum-oxo-hydroxo units, as confirmed by thermogravimetric analysis-mass spectrometry (TGA-MS), differential scanning calorimetry (DSC), and Fourier transform infrared spectroscopy (FTIR) studies (see Figures S1 and S2). Dynamic light scattering (DLS) data show that the average hydrodynamic radius is approximately 1 nm (see Figure S1). In this regard, it is important to note that Keggin-type aluminum oxyhydroxide nanoclusters are well-known in aqueous solution.³⁵ These cationic compounds with both Al_{13} and Al_{30} cores have sizes of 1 to 2 nm, which is consistent with our DLS results. Thus, the elemental composition of the oligomeric species prepared in this work might be similar to those reported in the literature. However, the fact that they are X-ray amorphous makes definitive assignments very difficult.

In the synthesis, AlCl_3 first reacts with ethanol to produce a complex compound with the probable composition of $\text{AlCl}_2(\text{OEt}) \cdot 2\text{AlCl}_3 \cdot 10\text{EtOH}$.³⁶ The hydroxylation process^{37–40} begins when benzyl alcohol is added to the mixture (see nuclear magnetic resonance (^1H NMR) and gas chromatography–mass spectrometry (GC-MS) data in Figure S3) according to



The heterolytic C–O bond cleavage is facilitated by the fact that the phenyl ring adjacent to the $\alpha\text{-C}$ atom is capable of delocalizing the positive charge via resonance (aromatic π -system), thereby stabilizing the carbocation.⁴¹ This is the reason why benzyl alcohol and other reagents, such as *tert*-amyl alcohol and 1-phenylethanol, are considered good oxygen donors for nonaqueous sol–gel synthesis of oxide nanoparticles.^{42,43} Aside from benzyl chloride shown in eq 2, other byproducts, including dibenzyl ether and benzyl ethyl ether, are also found in trace amounts due to etherification reactions (see Figure S3). The combination of moderate reaction temperature and 1,3-propanediol as a stabilizing ligand allows control of both the hydrolysis and condensation rates on the molecular level. This means that gel formation, which is sometimes observed in such synthesis routes, can be prevented under the

experimental conditions. We note, however, that higher reaction temperatures lead to gelation of the mixture due to an increase in the oligomer size (i.e., the degree of condensation). Lastly, FTIR data also confirm the presence of bridging hydroxyl groups in the oligomeric material (see Figure S2). Considering the fact that benzyl chloride is formed during synthesis, this result corroborates the proposed reaction pathway. Further details on the mechanism will be presented in a separate work.

Mesoporous $\eta\text{-Al}_2\text{O}_3$ thin films were fabricated using an EISA process.⁴⁴ This process was introduced in the late 1990s and is based on the solution phase coassembly of either preformed building blocks, such as nanoparticles, or molecular sol–gel precursors with a structure-directing agent.^{45–52} Breakthroughs over the last 10 years have made EISA the method of choice in the synthesis of thin film materials with periodicities in the sub-40 nm size range. In the ensuing section we establish that $\eta\text{-Al}_2\text{O}_3$ can be templated using different amphiphilic polymers, including commercially available triblock copolymers of the Pluronic family and more specialty templates, such as poly(ethylene-*co*-butylene)-*block*-poly(ethylene oxide) and polyisobutylene-*block*-poly(ethylene oxide) diblock copolymers, also referred to as KLE²⁵ and PIB-*b*-PEO_y, respectively, to produce high quality thin films with both cubic and hexagonal pore symmetries. We also demonstrate that the in-plane pore size is readily tunable from 10 to 30 nm by the choice of polymer.

Recently we have shown that 2-methoxyethanol as a cosolvent helps slow down the drying process of polymer-templated sol–gel derived thin films due to its “low” vapor pressure, which ultimately leads to materials with more ordered structures.^{53,54} In the present work, by contrast, we exploit the low reactivity of the aluminum-oxo-hydroxo building blocks and show that mesoporous thin films with exceptional order can be achieved at relative humidities of more than 80%. Such high humidities also slow down the drying of films during the EISA process in that they seem to remain in a quasi-fluid state; similar conditions are often not applicable to conventional synthesis routes due to the high reactivity of molecular sol–gel precursors with water.

To probe the nanostructure of the different $\eta\text{-Al}_2\text{O}_3$ thin films materials, scanning electron microscopy (SEM), transmission electron microscopy (TEM), and atomic force microscopy (AFM) were used. The combination of these techniques allows imaging of both the top surface of the films and the porous interiors. Figure 1 shows microscopy and electron diffraction (ED) data of KLE-templated $\eta\text{-Al}_2\text{O}_3$ samples heated to 900 and 1000 °C. Top view SEM and tapping mode AFM images reveal an ordered cubic network of open pores averaging 25 nm in diameter. This dimension is not typical of KLE-templated materials^{17,48,53,54} (25 nm vs ~16 nm) and is likely associated with the fact that unlike molecular sol–gel precursors, the oligomeric building blocks cannot penetrate into the micellar corona. SEM and AFM further show that the top surface is both flat and crack-free at the micrometer length scale and contains only minor structural defects (see also Figure S4). 2-Dimensional fast Fourier transform (2D-FFT) confirms the hexagonal symmetry of the top surface. From bright-field TEM and cross-sectional SEM, we are able to establish that the highly ordered pore structure observed at the solid/air interface persists throughout the films. Figure 1e is an ED pattern showing Debye–Scherrer rings characteristic of a material with randomly oriented nanocrystalline domains.

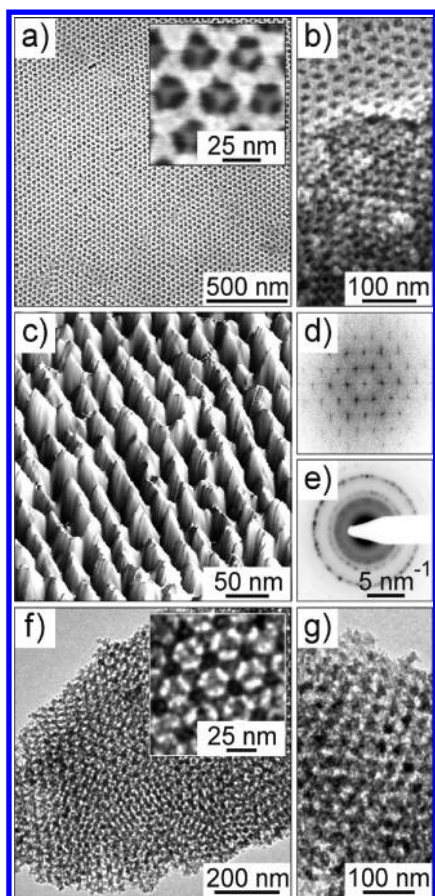


Figure 1. Morphology of KLE-templated η - Al_2O_3 thin films heated to 900 °C (a–f) and 1000 °C (g). (a) Top view SEM image showing open 25 nm diameter pores. A higher magnification SEM image is shown in the inset of part (a). (b) Cross-sectional SEM image of a cut in a film held at a tilt of 50°. (c) High-magnification 3D-AFM height image. The contrast covers height variations in the 1–6 nm range. (d) 2D-FFT image verifying the hexagonal symmetry of the top surface. (e) Selected area ED pattern showing Debye–Scherrer rings characteristic of nanocrystalline η - Al_2O_3 . (f,g) Low-magnification bright-field TEM images. A higher magnification TEM image is shown in the inset of part (f).

Calculated lattice spacings match best with the JCPDS (Joint Committee on Powder Diffraction Standards) reference card no. 1-077-0396 for η - Al_2O_3 with cubic defect spinel structure. Lastly, it is also evident from Figure 1 that annealing at 1000 °C only slightly disrupts the nanoscale periodicity, which emphasizes the thermal stability of the KLE-templated η - Al_2O_3 thin film.

As mentioned above, η - Al_2O_3 thin films can also be templated using other polymers but under otherwise similar conditions. Figure 2 shows low- and high-magnification TEM images of $\text{PIB}_{53}\text{-}b\text{-PEO}_{45}$,⁵⁵ $\text{PIB}_{107}\text{-}b\text{-PEO}_{100}$,⁵⁶ Pluronic F127-, and Pluronic P123-templated samples heated to 900 °C. While $\text{PIB}_{53}\text{-}b\text{-PEO}_{45}$ produces materials with a highly ordered honeycomb network of pores similar to that of KLE-templated thin films (see also Figure S4), the use of the large diblock copolymer $\text{PIB}_{107}\text{-}b\text{-PEO}_{100}$ as the structure-directing agent leads to materials with disordered pore-solid architectures reminiscent of foam-like structures. The average in-plane pore sizes are 20 and 30 nm, respectively. Because the $\text{PIB}_{107}\text{-}b\text{-PEO}_{100}$ diblock copolymer is not readily soluble in methanol, we decided to use tetrahydrofuran as a cosolvent to achieve

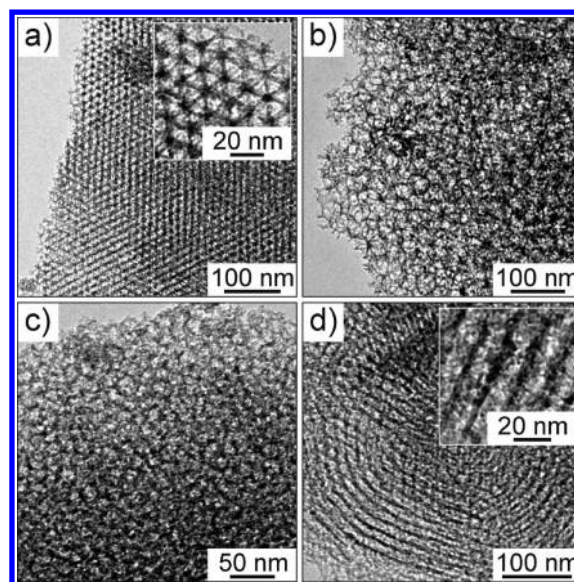


Figure 2. Low- and high-magnification bright-field TEM images of $\text{PIB}_{53}\text{-}b\text{-PEO}_{45}$ - (a), $\text{PIB}_{107}\text{-}b\text{-PEO}_{100}$ - (b), Pluronic F127- (c), and Pluronic P123-templated (d) η - Al_2O_3 thin films heated to 900 °C. The in-plane pore size is readily tunable from 10 to 30 nm, and both cubic and hexagonal mesoporous thin films can be produced by coassembly strategies.

isotropic dip-coating solutions. This might be the reason for the formation of foam-like structures. Although both solvents have similar boiling points, mixtures can interfere with the self-assembly process for solubility reasons.

Conventional triblock copolymers of the Pluronic family also produce well-defined thin films. The η - Al_2O_3 materials shown in Figure 2c and d were fabricated from a sol that was stored for more than one year in a sealed flask at ambient conditions, which underlines the long-term stability of dispersed aluminum-oxo-hydroxo building blocks. Both cubic and hexagonal pore symmetries and mesopore cavities ranging from 10 to 16 nm in diameter can be achieved by choosing the appropriate amount of polymer in the starting solution. A mass fraction of Pluronic P123 of 0.50 (here $m_{\text{polymer}}/m_{\text{polymer+oxide}}$) leads to the formation of hexagonal thin films, while Pluronic F127 seems to favor cubic pore symmetries up to a mass fraction of 0.67. We note, however, that the influence of the polymer mass fraction on the nanoscale structure of η - Al_2O_3 thin films was not investigated in detail in this work. The average pore wall thickness of the materials shown in Figure 2 is 5 nm, which is consistent with calculated values for the crystallite size (see section on X-ray diffraction below). This result therefore provides a hypothesis for understanding why the different mesoporous morphologies are retained when the crystalline phase is achieved.

In summary, the data in Figures 1 and 2 collectively verify that high quality η - Al_2O_3 thin films can be readily produced using an EISA process and amphiphilic block copolymers as the structure-directing agents.

The synthesis method employed in this work is also readily extendable to mesoporous powder materials and micrometer-sized beads with multimodal porosity. Figure 3a shows low- and high-magnification TEM images of a $\text{PIB}_{53}\text{-}b\text{-PEO}_{45}$ -templated powder sample heated to 900 °C. The average pore diameter is 14 nm, which is smaller compared to thin films prepared with the same diblock copolymer (see Figure 2a). Part of the reason

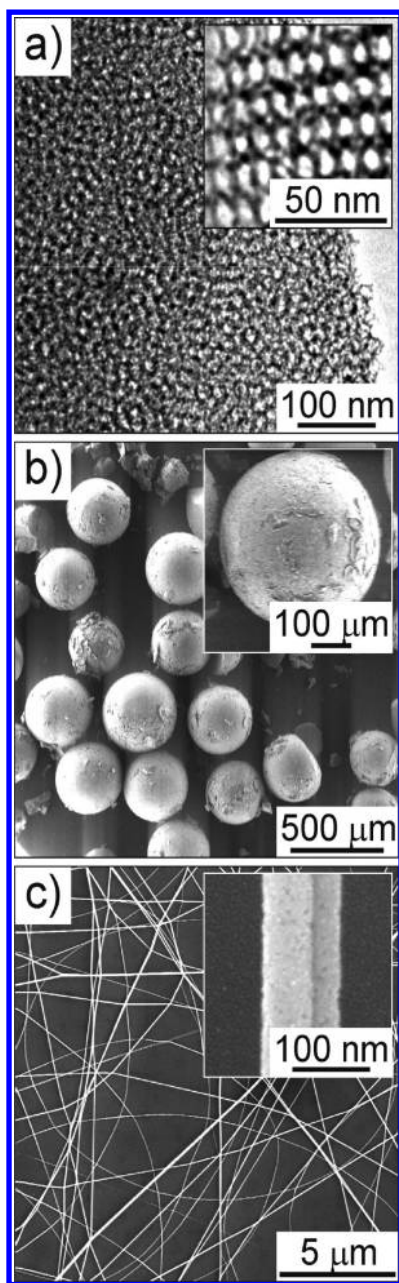


Figure 3. Morphology of different η - Al_2O_3 nanomaterials heated to 900 °C. (a) Bright-field TEM images of PIB_{53} - b - PEO_{45} -templated powder showing open pores averaging 14 nm in diameter. (b) SEM images of hierarchically porous microbeads prepared using Amberlite XAD-16 as the hard template. (c) SEM images of electrospun nanofibers.

for this is the different polymer mass fraction used to achieve materials with a well-defined mesoporous morphology. From Figure 3a, it can further be seen that η - Al_2O_3 samples in powder format have a lower degree of pore ordering, which might also be related to the different synthesis conditions.

As for hierarchically porous η - Al_2O_3 , we used commercially available Amberlite XAD-16 polystyrene beads as the hard templates instead of siliceous or carbonaceous materials, such as SBA-15 and CMK-3.^{27,28} Briefly, the micrometer-sized η - Al_2O_3 beads were prepared by incipient wetness impregnation method. Infiltration and drying was repeated twice and the obtained material calcined at 700 °C under nitrogen

atmosphere. The latter step is not vital for successful synthesis but helps retain both the macroscopic shape and porous morphology of the beads due to partial carbonization of the polystyrene template. Finally, removal of the organic constituents is achieved by heating the samples to temperatures above 700 °C in air. The SEM images in Figure 3b clearly show that the replica beads remain intact and seem to be mechanically stable after annealing at 900 °C.

Both the low reactivity and good redispersibility of the aluminum-oxo-hydroxo building blocks makes them also suitable for the fabrication of uniform nanofibers with high aspect ratio by electrospinning. In the synthesis, polyvinyl butyral was used as the carrier polymer to increase the viscosity of the spinning solution, and the flow rate was controlled by a syringe pump. Application of a strong electric field between the capillary containing the solution and the collector causes formation of a Taylor cone, which then emits a jet stream due to elongation of the liquid/air interface.^{29,30} The SEM images in Figure 3c show the rather dense structure of the η - Al_2O_3 nanofibers with 70 nm average diameter and a few tens of micrometers in length after annealing at 900 °C.

In the ensuing sections we specifically focus on the porous η - Al_2O_3 nanomaterials. More quantitative information on the structure of the polymer-templated thin films was obtained by grazing incidence small-angle X-ray scattering (GISAXS). Figure 4 shows GISAXS patterns at an angle of incidence

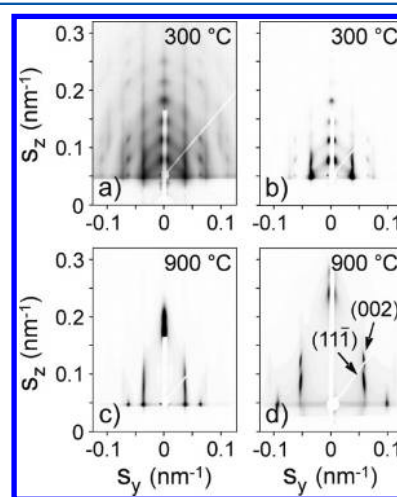


Figure 4. Synchrotron-based GISAXS on KLE-templated (a-c) and PIB_{53} - b - PEO_{45} -templated (d) thin films with amorphous and nanocrystalline pore wall structures. The pattern in (a) is plotted with logarithmic intensity scale to make all scattering maxima visible, while (b-d) have linear intensity scales. GISAXS data were collected at an angle of incidence $\beta = 0.2^\circ$ and show the evolution of the highly ordered f-c-c pore networks with (111) orientation upon thermal annealing. Scattering vector, s , components are given in nm^{-1} .

$\beta = 0.2^\circ$ collected on both KLE-templated and PIB_{53} - b - PEO_{45} -templated materials with amorphous and nanocrystalline frameworks. Samples with amorphous pore walls produce patterns with distinct scattering maxima that can be indexed to face-centered-cubic (f-c-c) close-packed structures with (111) orientation relative to the plane of the substrate. This pore orientation is consistent with results from electron microscopy (e.g., with the hexagonal top surface) and is further often observed for sol-gel derived oxide thin films templated using the large diblock copolymer KLE.^{17,53} The GISAXS pattern in

Figure 4a is plotted with logarithmic intensity scale to emphasize the exceptional pore ordering of the KLE-templated samples. Even seventh order reflections can be clearly observed in the off-plane direction, which is unusual for polymer-templated thin films, in particular large-pore mesoporous materials.

The elliptical shape of the scattering patterns in Figure 4 further indicates lattice contraction normal to the plane of the substrate. As expected, the in-plane contraction is negligible because the films are bound to the substrate. Based on the relative position of the (111) scattering maxima a decrease in volume of more than 70% is determined for samples heated to 900 °C. This volume contraction is associated with continuous pore transformation from spherical to oblate, as can be seen in the cross-sectional SEM image in Figure 1b. Higher annealing temperatures do not lead to further contraction (see Figure 5)

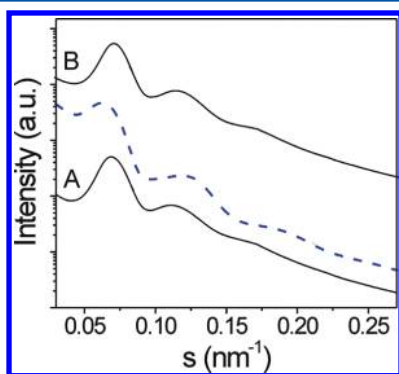


Figure 5. SAXS data obtained on PIB₅₃-*b*-PEO₄₅-templated powder heated to 900 (A) and 1000 °C (B). The dashed blue line is a fit to the data of (A).

because the materials are already highly crystalline by 900 °C. Also, unlike most mesoporous oxide thin films, no loss of out-of-plane scattering is observed after thermal treatment at 900 °C, thereby verifying both good in- and out-of-plane order. The reason for the lack of out-of-plane scattering is often due, in part, to the small number of repeat units normal to the plane of the substrate and the process of crystallizing the amorphous framework itself, which may disrupt the nanoscale periodicity.

Figure 5 shows both SAXS data obtained on PIB₅₃-*b*-PEO₄₅-templated powder heated to 900 and 1000 °C and a fit to the 900 °C data. Both SAXS curves show diffuse maxima typical of polymer-templated metal oxides with spherical mesopores. However, the data do not allow for a differentiation between the possible crystal structures (i.e., f-c-c, b-c-c, and h-c-p). While the first reflection can be assigned to the main Bragg peak, e.g., (111) in the case of an f-c-c structure, the subsequent modulations represent the superposition of both the form factor and the lattice factor. It is apparent from these data that samples in powder format have a somewhat lower pore ordering than the corresponding PIB₅₃-*b*-PEO₄₅-templated thin films. In addition, it can be clearly seen that the pore-solid architectures can effectively withstand the stresses that develop during the course of high temperature annealing.

To extract the mesopore size and the lattice parameter, the SAXS data were also analyzed using a theoretical model.⁵⁷ Here, we assumed an f-c-c lattice of spherical pores while taking into account lattice defects and a certain polydispersity, both of which account for the width of the diffuse maxima and minima. The shape of the SAXS curve can be reasonably modeled, as

shown in Figure 5. From the fit, we obtain an average mesopore size of (15.0 ± 1.2) nm and a lattice constant, a , of (18.6 ± 2) nm. These values are in agreement with results from TEM imaging (see Figure 3a) and physisorption (see Figure 6b).

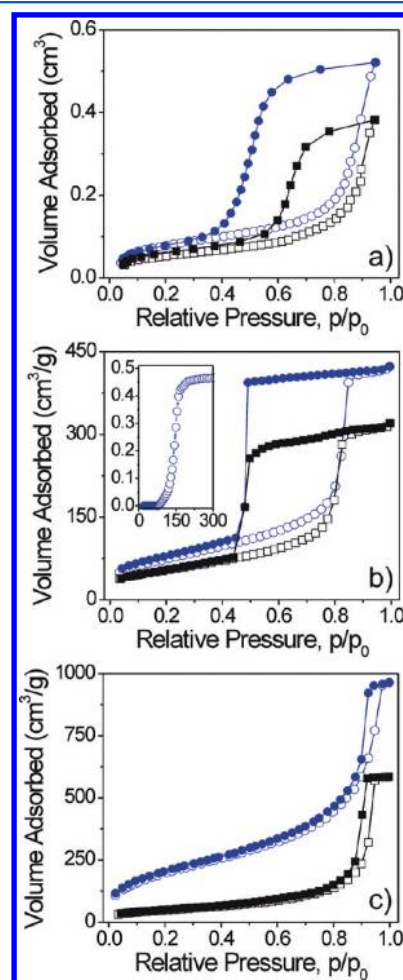


Figure 6. (a) Krypton physisorption isotherms of KLE-templated thin films with a total area of 56 cm² heated to 550 (blue circles) and 900 °C (black squares). The average film thickness is 250 and 200 nm, respectively. (b) Nitrogen physisorption isotherms of PIB₅₃-*b*-PEO₄₅-templated powder material heated to 550 (blue circles) and 900 °C (black squares). A cumulative pore volume plot (i.e., pore volume [cm³/g] vs pore size [Å]) for 900 °C is shown in the inset (NLDFT, adsorption branch model for cylindrical/spherical pores). (c) Nitrogen physisorption isotherms of Amberlite XAD-16 polystyrene beads (blue circles) and η -Al₂O₃ replica beads (black squares) heated to 900 °C.

The porous properties of the different Al₂O₃ nanomaterials were analyzed by gas physisorption in order to obtain information on both pore volume and specific surface area. Measurements on KLE-templated thin films with amorphous and nanocrystalline pore wall structures were carried out at 87 K using krypton as the adsorbate. Under these conditions, the saturation pressure, p_0 , is ~ 13 Torr (17.3 hPa). The reason for the use of krypton at 87 K instead of nitrogen at 77 K is the higher sensitivity of this technique. Pressure changes due to adsorption of nitrogen cannot be determined precisely for porous thin films because of the low amount of material involved and the high saturation pressure of nitrogen at its boiling point of 77 K.

Figure 6a shows type-IV isotherms characteristic of a material with open mesopore cavities that are interconnected through smaller necks. Both KLE-templated thin films heated to 550 and 900 °C show a distinct capillary condensation step at $p/p_0 = 0.85$. It is evident from these data that higher annealing temperatures lead to a reduction in pore volume and specific surface area. Part of the reason for this is the formation of nanocrystalline η - Al_2O_3 domains in the initially amorphous pore walls, which slightly disrupts the nanoscale porosity. We note that the shift of the lower hysteresis closure point is likely a result of the continuous lattice contraction upon thermal annealing (see Figure 4) and the crystallization process itself. Both lead to an altered pore geometry, which is known to have a profound effect on the desorption properties. Using a cross-sectional area of 20.5 Å² for krypton and taking into account the total area and average film thickness, pore volumes of $8.1 \cdot 10^{-4} \text{ cm}^3$ (equivalent to 58% porosity) and $5.9 \cdot 10^{-4} \text{ cm}^3$ (equivalent to 53% porosity) and Brunauer–Emmett–Teller (BET) surface areas of $255 \text{ m}^2 \cdot \text{cm}^{-3}$ and $218 \text{ m}^2 \cdot \text{cm}^{-3}$ are obtained for samples heated to 550 and 900 °C, respectively. These results confirm the high quality of the KLE-templated η - Al_2O_3 materials with uniform open pores persisting throughout the bulk of the films.

Figure 6b shows nitrogen adsorption–desorption isotherms of $\text{PIB}_{53}\text{-}b\text{-PEO}_{45}$ -templated powder heated to 550 and 900 °C. These isotherms provide ample evidence for the accessibility of the distorted cubic network of pores. The crystalline material exhibits a BET surface area of $200 \text{ m}^2 \cdot \text{g}^{-1}$ and a pore volume of $0.49 \text{ cm}^3 \cdot \text{g}^{-1}$. For amorphous samples, we find larger values of $270 \text{ m}^2 \cdot \text{g}^{-1}$ and $0.65 \text{ cm}^3 \cdot \text{g}^{-1}$, respectively. The cumulative pore volume plot in the inset of Figure 6b indicates a narrow pore size distribution centered at $\sim 15 \text{ nm}$, which is consistent with results from TEM imaging (see Figure 3a).

Lastly, we also examined the pore structure of η - Al_2O_3 materials prepared by the hard-templating method. Figure 6c shows nitrogen physisorption data of hierarchically porous Amberlite XAD-16 and η - Al_2O_3 replica beads heated to 900 °C. Commercially available Amberlite XAD-16 polystyrene beads have a BET surface area of $940 \text{ m}^2 \cdot \text{g}^{-1}$ and a pore volume of $1.9 \text{ cm}^3 \cdot \text{g}^{-1}$ after repeated washing with water and methanol. In contrast, the templated η - Al_2O_3 exhibits specific surface areas of $175 \text{ m}^2 \cdot \text{g}^{-1}$ and $140 \text{ m}^2 \cdot \text{g}^{-1}$ and pore volumes of $0.9 \text{ cm}^3 \cdot \text{g}^{-1}$ and $0.8 \text{ cm}^3 \cdot \text{g}^{-1}$ after annealing at 900 and 1000 °C, respectively. The reduction in both pore volume and BET surface area can be attributed to nanocrystalline domain growth (see Figure S5). However, the porosity values are still in a reasonable range for many applications. In this regard, we note that the η - Al_2O_3 replica beads cannot be directly compared to the Amberlite XAD-16 beads used as the hard templates for the following reasons. First, the pore networks are not identical in both materials since the η - Al_2O_3 pore structure is a negative replica of the polystyrene template. Second, the bulk density of η - Al_2O_3 ($3.66 \text{ g} \cdot \text{cm}^{-3}$ taken from JCPDS reference card no. 1-077-0396) is more than three times higher than that of polystyrene, and this deviation exerts a significant influence on the calculated surface area and pore volume since these data are normalized by weight.

Both the crystallization behavior and elemental composition of the different nanomaterials prepared in this work were examined in detail using wide-angle X-ray diffraction (WAXD) and X-ray photoelectron spectroscopy (XPS). Figure 7a shows WAXD patterns obtained on $\text{PIB}_{53}\text{-}b\text{-PEO}_{45}$ -templated powder heated to 700 °C, 800 °C, and 900 °C in air. From these data, it

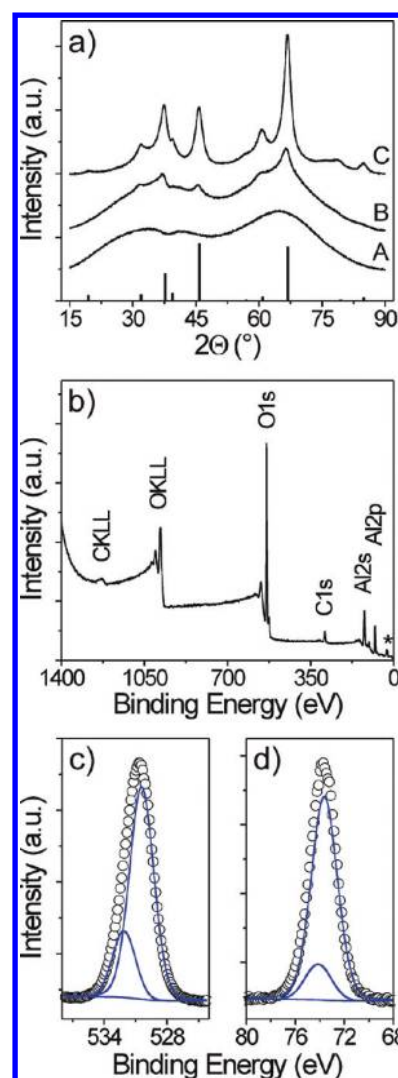


Figure 7. (a) WAXD patterns obtained on $\text{PIB}_{53}\text{-}b\text{-PEO}_{45}$ -templated Al_2O_3 powder heated to 700 °C (A), 800 °C (B), and 900 °C (C). The stick pattern shows JCPDS reference card no. 1-077-0396 for η - Al_2O_3 . (b) Typical XPS survey spectrum of a KLE-templated η - Al_2O_3 thin film on a (100)-oriented silicon wafer heated to 900 °C. The O2s region is indicated by an asterisk. The weak peaks on the left- and right-hand sides of the Al2s line can be attributed to silicon from the substrate. (c,d) High-resolution scans of the O1s and Al2p core levels. Blue lines are Gaussian–Lorentzian fits to the data assuming Shirley background.

can be clearly seen that the crystallization of the initially amorphous pore wall structure begins at temperatures above 700 °C. Similar behavior is observed for polymer-templated thin films, while the hierarchically porous beads seem to be already crystalline at 700 °C. In agreement with electron diffraction, the results with WAXD show that the materials studied here adopt the defect spinel structure of η - Al_2O_3 ; the positions of the diffraction peaks closely match the JCPDS reference card no. 1-077-0396. Applying the Scherrer equation to the full width at half-maximum intensity of the three most intense peaks in Figure 7a provides an average crystallite size of 4 nm. This dimension is in accordance with the pore wall thickness determined from SAXS and TEM and is further assumed to be the stable nanocrystalline domain size. Higher annealing temperatures only lead to a slight increase in crystallite size, which helps explain why thermal annealing at

1000 °C is not accompanied by the loss of nanoscale periodicity both for thin film and powder materials (see Figures 1d and 5). This result, however, also implies that the nanocrystalline domain size cannot be tuned to tailor the physical properties. Moreover, we find that prolonged annealing at 1150 °C results in conversion of η -Al₂O₃ to α -Al₂O₃ with 40 nm average crystallite size (see Figure S5). As mentioned above, corundum is the thermodynamically stable bulk phase of Al₂O₃. Interestingly, the same solid–solid conversion is already observed at approximately 900 °C for samples prepared with no polymer template, which shows the profound effect that nanoconfinement has on the thermal stability of the eta-alumina phase. Lastly, we note that the metastable transition phases of Al₂O₃, including γ -, η -, and δ -Al₂O₃, have very similar defect spinel structures. For this reason, they are difficult to distinguish by X-ray diffraction, especially if the crystalline domains are small and the material is likely to contain defects, such as lattice dislocations, and so forth. Thus, the presence of second phases cannot be fully ruled out on the basis of the diffraction data alone.

Figure 7b shows a typical XPS survey spectrum of a KLE-templated η -Al₂O₃ thin film on a (100)-oriented silicon wafer. Apart from a weak carbon C1s peak, which we associate with adventitious hydrocarbon, only aluminum, oxygen, and silicon core levels are observed. The appearance of silicon lines is presumably associated with diffusion of silicon across the interior of the film at high temperatures; mobile species are always enriched at interfaces due to surface energy minimization reasons. Figure 7c and d shows both high-resolution scans of the Al2p and O1s regions and fits to the data. The Al2p spectrum contains one peak at a binding energy of (73.65 ± 0.05) eV and another minor one at (74.14 ± 0.05) eV. The former component is assigned to aluminum in Al₂O₃, while the latter is assigned to surface Al–OH. The O1s spectrum shows a slightly asymmetric peak. Peak deconvolution reveals two different oxygen bonding states. The peak for oxygen in Al₂O₃ lies at (530.45 ± 0.05) eV, while the one for Al–OH is located at (532.14 ± 0.05) eV. Overall, the peak positions are consistent with reported measured values for alumina materials.^{58,59} In addition, the XPS results provide evidence that the nanocrystalline η -Al₂O₃ thin films are also well-defined at the atomic level.

A study of the catalytic properties of both the hierarchically porous microbeads and mesoporous powder materials is planned for the future. In this regard, it is important to note that the same η -Al₂O₃ systems could also be used as catalytic support materials due to their high thermal and mechanical stability. Moreover, it is envisioned that the porous η -Al₂O₃ nanomaterials studied in this work will facilitate the formation of novel composite catalysts with a high density of active sites.

CONCLUSIONS

In summary, we have reported a facile route to nanocrystalline η -Al₂O₃ materials with different morphologies by using preformed aluminum-oxo-hydroxo species as building blocks. These amorphous, oligomeric species can be synthesized in benzyl alcohol, which acts both as the solvent and oxygen donor, and further converted to η -Al₂O₃ at annealing temperatures above 700 °C.

Mesoporous thin film and powder materials with uniform pores ranging from 10 to 30 nm have been successfully prepared through coassembly strategies with various amphiphilic block copolymers as the structure-directing agents. The

use of aluminum-oxo-hydroxo building blocks also provides an efficient route to produce nanofibers with high aspect ratio by electrospinning and hierarchically porous beads by replication of Amberlite XAD-16 polystyrene beads. Electron microscopy, physisorption, SAXS, WAXD, and XPS studies collectively verify that the initially amorphous materials can be crystallized while retaining both the macroscopic shape and nanoscale structure. The structure and morphology results also indicate that the samples prepared in this work are not only homogeneous at the nanoscale but also at the micrometer level after annealing in air at temperatures as high as 1000 °C. Lastly, the present work shows the profound effect that nanoconfinement has on the thermal stability of the eta-alumina phase. From a broader perspective, this result indicates a new design paradigm for η -Al₂O₃ materials with significantly enhanced thermal stability.

ASSOCIATED CONTENT

Supporting Information

DLS, TGA-MS, DSC, ¹H NMR, GC-MS, FTIR, SEM, TEM, and WAXD data. This material is available free of charge via the Internet at <http://pubs.acs.org>.

AUTHOR INFORMATION

Corresponding Author

*E-mail: bernd.smarsly@phys.chemie.uni-giessen.de (B.M.S.), torsten.brezesinski@phys.chemie.uni-giessen.de (T.B.).

ACKNOWLEDGMENTS

The authors thank both Anneliese Heilig, Rainer Ostermann, Jan Perlich, and Ken-ichi Iimura for their assistance in materials preparation and measurements and the German synchrotron radiation facility HASYLAB at DESY for beamtime. Roman Zieba, Alexander Traut, and Cornelia Röger-Göpfert from BASF SE Ludwigshafen are gratefully acknowledged for the supply of PIB-*b*-PEO_y diblock copolymers.

REFERENCES

- (1) Levin, I.; Brandon, D. J. *Am. Ceram. Soc.* **1998**, *81*, 1995–2012.
- (2) Morterra, C.; Magnacca, G. *Catal. Today* **1996**, *27*, 497–532.
- (3) Lyubovsky, M.; Pfefferle, L. *Catal. Today* **1999**, *47*, 29–44.
- (4) Narui, K.; Yata, H.; Furuta, K.; Nishida, A.; Kohtoku, Y.; Matsuzaki, T. *Appl. Catal., A* **1999**, *179*, 165–173.
- (5) Frank, B.; Emig, G.; Renken, A. *Appl. Catal., B* **1998**, *19*, 45–57.
- (6) Knozinger, H.; Ratnasamy, P. *Catal. Rev.: Sci. Eng.* **1978**, *17*, 31–70.
- (7) Trombetta, M.; Busca, G.; Rossini, S.; Piccoli, V.; Cornaro, U.; Guercio, A.; Catani, R.; Willey, R. J. *J. Catal.* **1998**, *179*, 581–596.
- (8) MacIver, D. S.; Wilmot, W. H.; Bridges, J. M. *J. Catal.* **1964**, *3*, 502–511.
- (9) McHale, J. M.; Aurox, A.; Perrotta, A. J.; Navrotsky, A. *Science* **1997**, *277*, 788–791.
- (10) Wefers, K.; Misra, C. *Oxides and Hydroxides of Aluminum*; Alcoa Research Laboratories: 1987.
- (11) Zhang, Z. R.; Hicks, R. W.; Pauly, T. R.; Pinnavaia, T. J. *J. Am. Chem. Soc.* **2002**, *124*, 1592–1593.
- (12) Zhang, Z. R.; Pinnavaia, T. J. *J. Am. Chem. Soc.* **2002**, *124*, 12294–12301.
- (13) Ji, L.; Lin, J.; Tan, K. L.; Zeng, H. C. *Chem. Mater.* **2000**, *12*, 931–939.
- (14) Sominska, E.; Cina, B.; Chaim, R.; Gedanken, A. *J. Am. Ceram. Soc.* **2000**, *83*, 89–94.
- (15) Kim, P.; Kim, Y.; Kim, H.; Song, I. K.; Yi, J. *Appl. Catal., A* **2004**, *272*, 157–166.
- (16) Xia, Y. D.; Mokaya, R. *J. Mater. Chem.* **2005**, *15*, 3126–3131.

- (17) Kuemmel, M.; Grosso, D.; Boissiere, U.; Smarsly, B.; Brezesinski, T.; Albouy, P. A.; Amenitsch, H.; Sanchez, C. *Angew. Chem., Int. Ed.* **2005**, *44*, 4589–4592.
- (18) Boissiere, C.; Nicole, L.; Gervais, C.; Babonneau, F.; Antonietti, M.; Amenitsch, H.; Sanchez, C.; Grosso, D. *Chem. Mater.* **2006**, *18*, 5238–5243.
- (19) Zhou, S. X.; Antonietti, M.; Niederberger, M. *Small* **2007**, *3*, 763–767.
- (20) Yuan, Q.; Yin, A. X.; Luo, C.; Sun, L. D.; Zhang, Y. W.; Duan, W. T.; Liu, H. C.; Yan, C. H. *J. Am. Chem. Soc.* **2008**, *130*, 3465–3472.
- (21) Morris, S. M.; Fulvio, P. F.; Jaroniec, M. *J. Am. Chem. Soc.* **2008**, *130*, 15210–15216.
- (22) Sohlberg, K.; Pantelides, S. T.; Pennycook, S. J. *J. Am. Chem. Soc.* **2001**, *123*, 26–29.
- (23) Zhang, Z. R.; Pinnavaia, T. J. *Angew. Chem., Int. Ed.* **2008**, *47*, 7501–7504.
- (24) Shchukin, D. G.; Caruso, R. A. *Chem. Mater.* **2004**, *16*, 2287–2292.
- (25) Thomas, A.; Schlaad, H.; Smarsly, B.; Antonietti, M. *Langmuir* **2003**, *19*, 4455–4459.
- (26) Ryoo, R.; Joo, S. H.; Jun, S. J. *Phys. Chem. B* **1999**, *103*, 7743–7746.
- (27) Yang, H. F.; Zhao, D. Y. *J. Mater. Chem.* **2005**, *15*, 1217–1231.
- (28) Lu, A. H.; Schuth, F. *Adv. Mater.* **2006**, *18*, 1793–1805.
- (29) Li, D.; Xia, Y. N. *Adv. Mater.* **2004**, *16*, 1151–1170.
- (30) Greiner, A.; Wendorff, J. H. *Angew. Chem., Int. Ed.* **2007**, *46*, 5670–5703.
- (31) Mutin, P. H.; Vioux, A. *Chem. Mater.* **2009**, *21*, 582–596.
- (32) Niederberger, M.; Bard, M. H.; Stucky, G. D. *J. Am. Chem. Soc.* **2002**, *124*, 13642–13643.
- (33) Pinna, N.; Niederberger, M. *Angew. Chem., Int. Ed.* **2008**, *47*, 5292–5304.
- (34) Niederberger, M.; Garnweitner, G. *Chem.—Eur. J.* **2006**, *12*, 7282–7302.
- (35) Casey, W. H. *Chem. Rev.* **2006**, *106*, 1–16.
- (36) Mehrotra, R. K.; Mehrotra, R. C. *Z. Anorg. Allg. Chem.* **1961**, *311*, 198–202.
- (37) Arnal, P.; Corriu, R. J. P.; Leclercq, D.; Mutin, P. H.; Vioux, A. *J. Mater. Chem.* **1996**, *6*, 1925–1932.
- (38) Vioux, A. *Chem. Mater.* **1997**, *9*, 2292–2299.
- (39) Ridge, D.; Todd, M. J. *Chem. Soc.* **1949**, 2637–2640.
- (40) Corriu, R. J. P.; Leclercq, D.; Lefevre, P.; Mutin, P. H.; Vioux, A. *J. Non-Cryst. Solids* **1992**, *146*, 301–303.
- (41) Poverenov, E.; Leituss, G.; Milstein, D. *J. Am. Chem. Soc.* **2006**, *128*, 16450–16451.
- (42) Gerrard, W.; Woodhead, A. H. *J. Chem. Soc.* **1951**, 519–522.
- (43) Trentler, T. J.; Denler, T. E.; Bertone, J. F.; Agrawal, A.; Colvin, V. L. *J. Am. Chem. Soc.* **1999**, *121*, 1613–1614.
- (44) Brinker, C. J.; Lu, Y. F.; Sellinger, A.; Fan, H. Y. *Adv. Mater.* **1999**, *11*, 579–585.
- (45) Kresge, C. T.; Leonowicz, M. E.; Roth, W. J.; Vartuli, J. C.; Beck, J. S. *Nature* **1992**, *359*, 710–712.
- (46) Ciesla, U.; Schuth, F. *Microporous Mesoporous Mater.* **1999**, *27*, 131–149.
- (47) Choi, S. Y.; Mamak, M.; Coombs, N.; Chopra, N.; Ozin, G. A. *Adv. Funct. Mater.* **2004**, *14*, 335–344.
- (48) Smarsly, B.; Grosso, D.; Brezesinski, T.; Pinna, N.; Boissiere, C.; Antonietti, M.; Sanchez, C. *Chem. Mater.* **2004**, *16*, 2948–2952.
- (49) Ba, J. H.; Polleux, J.; Antonietti, M.; Niederberger, M. *Adv. Mater.* **2005**, *17*, 2509–2512.
- (50) Hoffmann, F.; Cornelius, M.; Morell, J.; Froba, M. *Angew. Chem., Int. Ed.* **2006**, *45*, 3216–3251.
- (51) Sanchez, C.; Boissiere, C.; Grosso, D.; Laberty, C.; Nicole, L. *Chem. Mater.* **2008**, *20*, 682–737.
- (52) Soler-illia, G. J. D.; Sanchez, C.; Lebeau, B.; Patarin, J. *Chem. Rev.* **2002**, *102*, 4093–4138.
- (53) Haetge, J.; Suchomski, C.; Brezesinski, T. *Inorg. Chem.* **2010**, *49*, 11619–11626.
- (54) Haetge, J.; Hartmann, P.; Brezesinski, K.; Janek, J.; Brezesinski, T. *Chem. Mater.* **2011**, *23*, 4384–4393.
- (55) von Graberg, T.; Hartmann, P.; Rein, A.; Gross, S.; Seelandt, B.; Roger, C.; Zieba, R.; Traut, A.; Wark, M.; Janek, J.; Smarsly, B. M. *Sci. Technol. Adv. Mat.* **2011**, *12*, 025005.
- (56) Wang, Y. D.; Brezesinski, T.; Antonietti, M.; Smarsly, B. *ACS Nano* **2009**, *3*, 1373–1378.
- (57) Kuang, D. B.; Brezesinski, T.; Smarsly, B. J. *Am. Chem. Soc.* **2004**, *126*, 10534–10535.
- (58) Chambers, S. A.; Droubay, T.; Jennison, D. R.; Mattsson, T. R. *Science* **2002**, *297*, 827–831.
- (59) Jakschik, S.; Schroeder, U.; Hecht, T.; Krueger, D.; Dollinger, G.; Bergmaier, A.; Luhmann, C.; Bartha, J. W. *Appl. Surf. Sci.* **2003**, *211*, 352–359.